Original Article

Brain Tumor Stages Prediction using FMS-DLNN Classifier and Automatic RPO-RG Segmentation

R. Sakthi Prabha[1], M. Vadivel[2]

[1]Department of Electronics and Communication Engineering, Sathyabama Institute of Science and Technology, Chennai
[2]Department of Electronics and Communication Engineering, Vidya Jyothi Institute of Technology, Hyderabad, Telangana

[1]Corresponding Author: rshakthi1990@gmail.com

Abstract - Recently, one amongst the deadliest diseases is Brain Tumor (BT). A cluster of abnormal cells, which are clustered around the brain's inner portion, is contained by the tumour. It amplifies the Intra cranial pressure; thus, the tumour cell growth mounts, leading to death. Hence, diagnosing BTs at an early stage is desirable. For BT-type classification, various ideas are suggested by the prevailing techniques. However, they did not concentrate on the stages of BT. This research aims to predict the tumour's stages utilizing Range Pelican Optimization-based Region Growing (RPO-RG) segmentation and Fuzzy Memorized and SigTan-based Deep Learning Neural Network (FMS-DLNN) classifier. Primarily, the Gaussian Kernelized Kuwahara Filter (GKKF) pre-processed the input MRI images. Utilizing the Enhanced Farthest First Clustering (EFFC) algorithm, the noise-removed image is clustered. After that, the tumor region is segmented by the RPO-RG algorithm. After segmentation, features are extracted; also, by utilizing the Logarithmic Fisher Discriminant Analysis (LFDA), the features' dimensionality is reduced. Lastly, for classifying the BT stages, the necessary features are given to FMS-DLNN. With the prevailing approaches, the proposed mechanism is analogized. The experimental assessment exhibits that the proposed system was more efficient in classifying the various stages of tumours.

Keywords - Deep learning, Magnetic Resonance Imaging (MRI), Brain tumor, Segmentation, Fuzzy Memorized and Sigtan-Deep Learning Neural Network (FMS-DLNN), Clustering.

1. Introduction

In the brain, the cells' uncontrolled and unnatural growth is named BTs, which could be categorized as primary tumours and secondary tumours. The tumours present in the brain tissue are named primary tumours, whereas the secondary tumours expand as the human body's other parts to the brain tissue via the bloodstream (Kang et al., 2021). Changes in mood and personality, difficulties in walking, headaches, trouble speaking, vomiting, and high blood pressure are the BTs' major symptoms (Amin et al., 2020). BTs could be categorized into 4 grades, as per the World Health Organization (WHO). The lower-level tumours are described by the grade 1 and grade 2 tumours, whereas the more severe ones are included in grade 3 and grade 4 tumours (Nadeem et al., 2020).

For a BT, the threat level relies on several factors, namely behavior, location, tumour style, size, and growth status. For identifying the tumour's size, growth, and location, along with behavior, radiological evaluation and estimation, are wielded once a BT is suspected. Regarding this information, treatments, namely chemotherapy, surgery, radiation, best therapy, et cetera, could be taken (Islam et al., 2021). In treatment, a faster response is implied by the earlier BT diagnosis. This aids in enhancing the patient's survival rate (Hatamizadeh et al., 2022). Magnetic Resonance Imaging (MRI), a popular non-invasive approach, generates various sorts of tissue contrast; also, radiologists have broadly wielded it for diagnosing BTs.

Generally, the neurologist manually segments the abnormal regions at every MR-imaging modality slice. However, the BTs' manual segmentation of MRI images is subjective and time-consuming (A. R. Khan et al., 2021) (Niu et al., 2020). Thus, designing automatic along with robust BT diagnosis mechanisms is desirable (Zhou et al., 2020). For the BTs' prediction and treatment, various image-processing models have been utilized. For predicting more accurately, excellent benefits were had by the MRI brain image segmentation on software-centred medical image evaluation (Karayegen & Aksahin, 2021). Brain Tumor Segmentation (BTS) systems are wielded in distinguishing tumour-infected tissues from healthy ones. By classifying the pixels, BT image segmentation is attained in numerous BTS applications; hence, the segmentation issue turns into a classification (Díaz-Pernas et al., 2021).

For BT detection, numerous Machine Learning (ML) approaches like linear regression, random forest, Fuzzy C-Means (FCM), K-Nearest Neighbor (KNN), et cetera have been developed. To decrease manual interactions in the medical field, these frameworks are wielded. In ML, accurate tumour detection is a complex task due to the tumor location and appearance variability. The Deep Learning (DL) techniques' application has a significant opportunity for predicting BTs with high accuracy together with reliability. This has surpassed the conventional ML approaches. In BT diagnosis, DL mechanisms have become popular; also, in image analysis fields, their performance is superior.

1.1. Problem Definition

Many DL-centric techniques have been developed for BT classification, but several challenges remain unresolved. They are listed below,

- Manual segmentation requires more time, which results in deviations in segmentation results.
- The prevailing approaches had restrictions on important information loss, which made the system inefficient.

Thus, motivated by these factors, this work aims to predict the tumour's stages utilizing a novel RPO-RG segmentation algorithm and FMS-DLNN classifier. The proposed technique's contributions are,

- To preserve the information from the noise removal process utilizing a novel pre-processing stage.
- To automatically segment the BT regions utilizing the RPO-RG algorithm.
- To accurately predict the stages of cancer utilizing the FMS-DLNN classifier.

The structure of this paper is arranged as follows: the related works are discussed in section 2; the proposed technique is explicated in section 3; the results and discussions are elucidated in section 4; lastly, the paper is winded up in section 5.

2. Literature Survey

(Noreen et al., 2020) established a multi-level feature extraction and concatenation technique for BT's early diagnosis. For BT detection, together with its classification, the pre-trained DL approaches utilized were Inception-v3 and DensNet201. The outcomes portrayed that the model produced excellent testing accuracy. The approach's main flaws were excessive processing power and time consumption.

(Gumaei et al., 2019) propounded an automated system to classify brain cancers by utilizing Normalized Prostate Cancer Antigen-Gastrointestinal Stromal Tumor (PCA-NGIST). For extracting the significant features of brain images, this model

was wielded. The outcomes illustrated that the model's accuracy was better when analogized with the prevailing approaches. However, it required a lot of training data, which was expensive to compute, and required a lot of time to train.

(Shah et al., 2022) recommended a fine-tuned deep Convolutional Neural Network (CNN) Efficient-B0 base system to classify and detect BT images. The model was fine-tuned with recommended layers that replaced prevailing invasive BT classification and enriched overall classification accuracy. The model outperformed other CNN models. However, the recommended approach lacks precision and consumes time.

(Ali et al., 2020) elucidated a model for segmenting the tumour from multimodal MRI scans by utilizing multiple 3D CNN models. The model achieved lower results than prevailing approaches regarding comparative dice scores attained via the BraTS server, although the multimodal MRI scan ensemble generated BTs' accurate segmentation.

(Deng et al., 2020) suggested DL approaches employed in an amalgamated scheme for attaining the appearance along with spatial accuracy results via Conditional Radom Fields (CRF) together with Heterogeneous CNN (HCNN). Initially, the image patch trained the HCNN. Then, by employing an image sliced with HCNN's fixed variables, the CRF was trained with CRF-Recurrent Regression-centered Neural Network (RRNN). The outcomes exhibited that the model could attain performance. However, the model took only a fixed-sized input and output for any task.

(Sharif et al., 2020) established an active DL-centric feature selection mechanism for segmenting and recognizing BTs. The outcomes displayed that a contrast enhancement step aided a better saliency map's construction. This better saliency map segmented the tumor region. But, accurate classification was not always required for all extracted combination features.

(Nagaraj et al., 2020) suggested a BT images' multi-classification utilizing a deep neural network. For classifying various BT, this technique was wielded. The technique's structure could not be reutilized for classifying a small number of images, although it has a higher accuracy. This was the limitation here.

(M. A. Khan et al., 2020) presented an automated multimodal classification framework for BT-type classification. The procedure included linear contrast stretching; DL features extraction; a joint learning methodology with Extreme Learning Machine (ELM); the Partial Least Square (PLS); lastly, the ELM-centered classification.
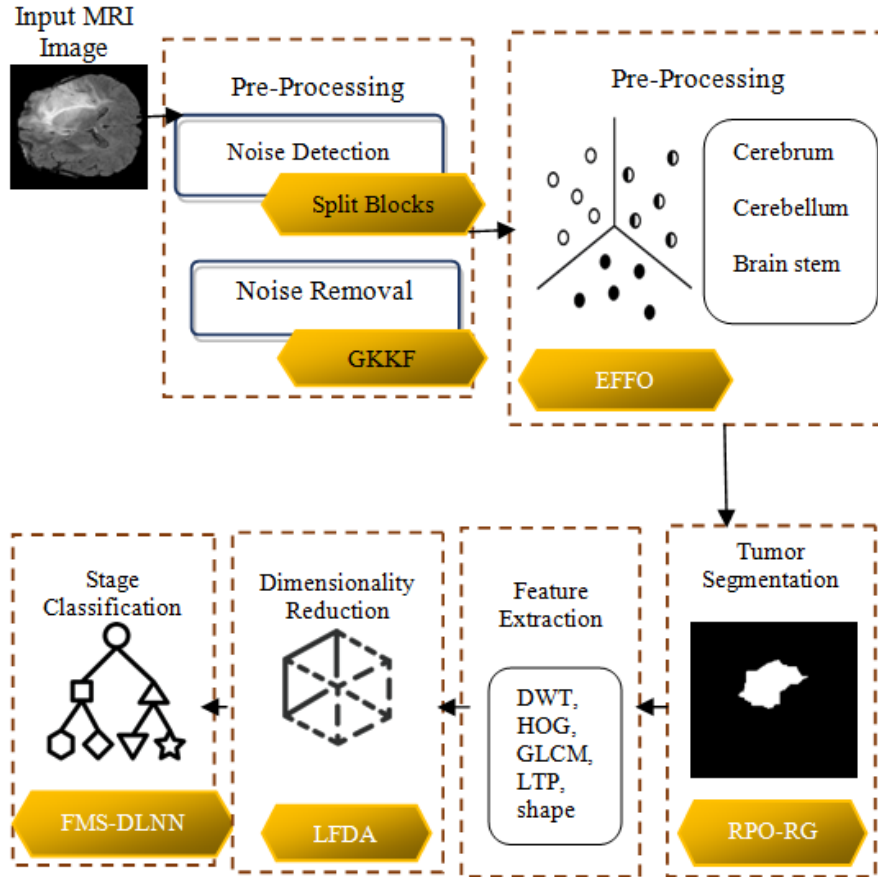
Fig. 1 Block diagram for the proposed methodology

The outcome illustrated that although the feature selection procedure was useful in enhancing the classification accuracy, it may require high complexity of the Hidden Layer (HL).

(Cristin et al., 2021) propounded an efficient classification technique, the so-called fractional-Chicken Swarm Optimization (fractional-CSO), for performing the severity-level tumor classification. For training the RNN classifier by simulating hierarchical order and behavior, this model was wielded. The result portrayed that the technique clearly distinguished the tumor as normal and abnormal. But, owing to the poor tuning of the Mother Hens (MN), Hens (HN), along with Roosters (RN), the approach might get stuck in local optima.

(Kesav & Jibukumar, 2022) presented an effectual along with the low-complex architecture for the BT classification along with prediction utilizing Regional-centric CNN (R-CNN) with two-channel CNN. Initially, a Two Channel CNN was utilised to classify betwixt the Glioma and healthy tumour MRI samples. After that, it was wielded as the R-CNN's feature extractor for detecting the Glioma MRI sample's tumour regions. The outcomes portrayed that the model could be capably wielded in classifying and detecting tumor types.

Nevertheless, the technique was limited to object detection.

(Harish & Baskar, 2020) presented a strategy for detecting and classifying tumors grounded on MR images utilizing Enhanced Faster R-CNN. To detect the BT, this model was wielded, which accurately separated the tumor area from non-tumor regions. The technique took longer to train the network, although it attained higher accuracy.

(Vidyarthi et al., 2022) proffered a huge feature set from 6 domains for capturing the major hidden information in the interest's extracted region. Then, utilizing the Cumulative Variance Method (CVM), the relevant features were extracted from the feature set pool. The outcomes exposed that the technique attained higher accuracy. However, with several publically accessible imaging datasets that have abnormality characteristics, the framework was not tested.

(Abdel-Gawad et al., 2020) developed an optimized edge recognition strategy regarding a genetic approach for detecting the BT's edges as of a patient's MR scan brain image. With the suitable training dataset, the technique was implemented.
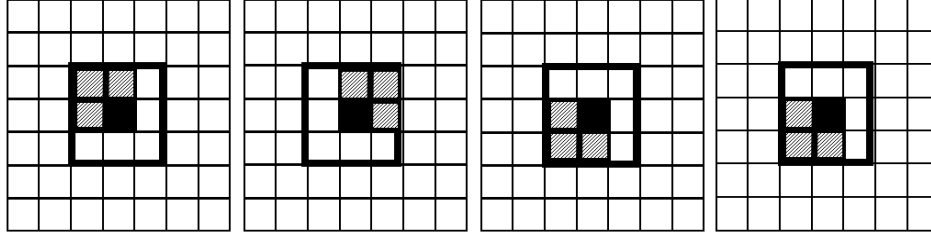
Fig. 2 Four areas of GKKF

The outcomes exhibited that when analogized with the prevailing and fractional-order edge detection mechanisms, the model exhibited better performance. But, the detections' accuracy relied majorly on the selected training images.

(Amin et al., 2019) expounded a BTS technique and classification grounded on score-level fusion utilizing transfer learning. Here, the segmented images were given to a pre-trained CNN system where feature learning was accomplished via Alex net together with Google net. The experimental observation displayed that the model yielded better outcomes on MRI/CT images. The limitation was whether it would work if the initial and target issues were alike for the first round of training to be relevant.

3. Proposed Brain Tumor Stages Prediction Framework

Here, a novel approach is proposed to predict the stages of BT utilizing RPO-RG segmentation and the FMS-DLNN classifier. Primarily, the GKKF technique removed the noise detected in the input image. After that, the brain part is clustered into three parts utilizing the EFFC algorithm. RPO-RG segmentation is executed in the clustered image for segmenting the tumour region. The features are extracted as of the segmented image; also, their dimensionality is reduced by the LFDA method. Lastly, the FMS-DLNN classifier is utilized to perform the various BT stages prediction. Figure 1 displays the block diagram for the proposed framework.

3.1. Pre-Processing

Pre-processing is the initial step to enhance the image's quality and make it fit the ML model. Here, the input MRI image($\Re$) taken as of the dataset is pre-processed utilizing split blocks and noise removal.

3.1.1. Noise Detection

Initially, the input image is split into blocks, and the intensity level of pixels in each block is measured. If the pixel's intensity level is maximum (i.e., 255), then it is indicated that the pixel has salt noise; also, if the pixel's intensity level is minimum (i.e., 0), then it is denoted that the pixel has pepper noise. The intensity's other levels are regarded as noise-free pixels. But, the maximum, as well as minimum intensities are not always presumed to be noise. So, the correlation is calculated betwixt the block's neighboring

pixels; also, the pixel has noise if the correlated value is lesser than the pre-assumed value. The correlation betwixt the neighboring pixels $\left(\varsigma_{\alpha\beta}\right)$ is expressed as,

$$\varsigma_{\alpha\beta} = \frac{\sum(\alpha_i - \overline{\alpha})(\beta_i - \overline{\beta})}{\sqrt{\sum(\alpha_i - \overline{\alpha})^2 \sum(\beta_i - \overline{\beta})^2}} \tag{1}$$

Where, α and β signifies the neighboring pixels. The pixel intensity level is considered noise-free if it is 0. Also, it is considered noisy if it is 0 and the average neighborhood level is not 0. Similarly, the same process is considered for the pixel intensity level of 255. The noise detection is expressed as,

$$\Re_{noise} = \begin{cases} 1, if \Re noisy \\ 0, if \Re noise free \end{cases} \tag{2}$$

Where, the input image is specified as $\Re$; also, the noise-detected image is represented as $\Re_{noise}$.

3.1.2. Noise Removal

Here, the GKKF removed the noise as of the noise-detected image ($\Re_{noise}$). The Kuwahara, which aids in adaptive noise removal of the images, is a non-linear type filter. For different window sizes, this filter is constructed. However, it has a problem of edge loss. To overcome this issue, the proposed methodology utilizes the Gaussian kernelized function instead of utilizing a general function. This modified noise removal process preserves the information more than the conventional noise removal methodologies. Initially, the filter is split into 4 various areas. The dark black color symbolizes the center pixel. Figure 2 illustrates the divided areas.

After that, the average and variance are computed for all four areas. The output value is defined as the mean of the sub-grid that presents the least variation, which is assigned to each area's central pixel. They are computed utilizing the following equations,

$$\nu_K = \frac{1}{(H+1)\times(H+1)}\sum(a,b) \in K \, G\big(\Re_{noisy}(a,b),\partial\big) \tag{3}$$

$$\sigma_K^2 = \frac{1}{(H+1)\times(H+1)}\sum(a,b) \in K \left[G\big(\Re_{noisy}(a,b),\partial\big) - \nu_K\right]^2 \tag{4}$$

Where, ν_K and σ_K^2 signifies the average and variance, correspondingly, the number of pixels in the current area is indicated as H, K signifies the four different regions $(0,1,2,3)$, $\Re_{noisy}(a,b)$ is the noisy images with (a,b) co-ordinates, and the Gaussian kernel function is exhibited as G, which can be represented as,

$$G\big(\Re_{noisy}(a,b),\partial\big) = \frac{1}{\sqrt{2\pi*\partial}} e^{-\frac{\big(\Re_{noisy}(a,b)\big)^2}{2\partial^2}} \qquad (5)$$

Where, ∂ is the width of the Gaussian kernel. Thus, the unnecessary noise detected in the input image is removed; also, the noise-free image is symbolized as $\Re_{pre}$.

3.2. Clustering

Initially, the first center is computed by the algorithm. The second center is selected as the point farthest from the first. By choosing the point farthest from the set of already selected centroids, every single remaining center is determined; also, the remaining points are added to the cluster whose center is the closest. The first center point is calculated by,

$$\hbar_{a,b} = \frac{\sum(a_i-\overline{a})(b_i-\overline{b})}{A-1} \qquad (6)$$

Wherein, the covariance value, that is, the first centroid of the points a and b is indicated as $\hbar_{a,b}$, A is the total number of points. After that, the remaining points are assigned to the cluster center $(\hbar)$ grounded on the similarity along with the distance from the center. The distance can be calculated by utilizing taxicab distance (τ) as,

$$\tau = \left|\Re_{pre_{n+1}} - \Re_{pre_n}\right| + |\hbar_{i+1} - \hbar_i|, n = 1,2,\ldots,A, i = 1,2,\ldots,\aleph \qquad (7)$$

By considering the minimum distance and similarities, the brain part is categorized into three clusters. The formed clusters are denoted as,

$$\aleph = \{\aleph_1, \aleph_2, \aleph_3\} \qquad (8)$$

Where, $\aleph$ is the output image containing the three clusters, and $\aleph_1$, $\aleph_2$, and $\aleph_3$ symbolizes the clusters of cerebrum, cerebellum, and brain stem, correspondingly.

3.3. Segmentation
3.3.1. Automatic Seed Generation

RPO is utilized as the automatic seed-generating technique, which finds the seed pixels in the brain region grounded on the pelican's behavior. The prevailing Pelican optimization algorithm provides better performance; however, it exhibits poor searching capability. To enhance their searching capability, the proposed system generates a range value concerning the population, and the value is multiplied during the population initialization. The range value is computed regarding the tent chaotic operator by the following expression,

$$\lambda_{i+1} = \begin{cases} \frac{\lambda_i}{0.7}, \lambda_i \le 0.7 \\ \frac{1-\lambda_i}{0.3}, \lambda_i > 0.7 \end{cases} \qquad (9)$$

Where, λ_i exemplifies the tent's chaotic sequence. In RPO, every single seed pixel indicates a candidate solution to the optimization issue whose position in the search space produces the decision variables' values. The population members, that is, the pixels, are initialized grounded on the problem's lower and upper bounds as described below,

$$\aleph_{i,j} = L_j + rand * \big(U_j - L_j\big) * \lambda_{i+1}, i = 1,2,\ldots,N, j = 1,2,\ldots,d \qquad (10)$$

Where, the value of the jth decision variable of the ith seed pixel is specified as $\aleph_{i,j}$, the lower and upper bounds are exemplified as L_j and U_j, correspondingly, the random number of range $[0, 1]$ is denoted as $rand$, the total number of seed pixels is exhibited as N, the number of decision variables is signified as d. Now, utilizing a matrix called the population matrix, the members are identified. The matrix is expressed as,

$$\aleph = \begin{bmatrix} \aleph_1 \\ \vdots \\ \aleph_i \\ \vdots \\ \aleph_N \end{bmatrix}_{N\times d} = \begin{bmatrix} \aleph_{1,1} \cdots \aleph_{1,j} \cdots \aleph_{1,d} \\ \vdots \ddots \vdots \ddots \vdots \\ \aleph_{i,1} \cdots \aleph_{i,j} \cdots \aleph_{i,d} \\ \vdots \ddots \vdots \ddots \vdots \\ \aleph_{N,1} \cdots \aleph_{N,j} \cdots \aleph_{N,d} \end{bmatrix}_{N\times d} \qquad (11)$$

Where, $\aleph_i$ indicates the ith seed pixel of the population. Now, for every candidate solution, the objective function is computed. The objective function's vector (X) can be defined as,

$$X = \begin{bmatrix} X_1 \\ \vdots \\ X_i \\ \vdots \\ X_N \end{bmatrix}_{N\times 1} = \begin{bmatrix} X(\aleph_1) \\ \vdots \\ X(\aleph_i) \\ \vdots \\ X(\aleph_N) \end{bmatrix}_{N\times 1} \qquad (12)$$

Where, the objective function value of the ith seed pixel is exemplified as X_i. The seed pixel that has the best objective function value is regarded as the best solution. The fitness value is grounded on the classifier's accuracy and centered on the pelicans' strategy. The candidate solutions are updated. They are imitated in two stages, namely the exploration and exploitation phases.
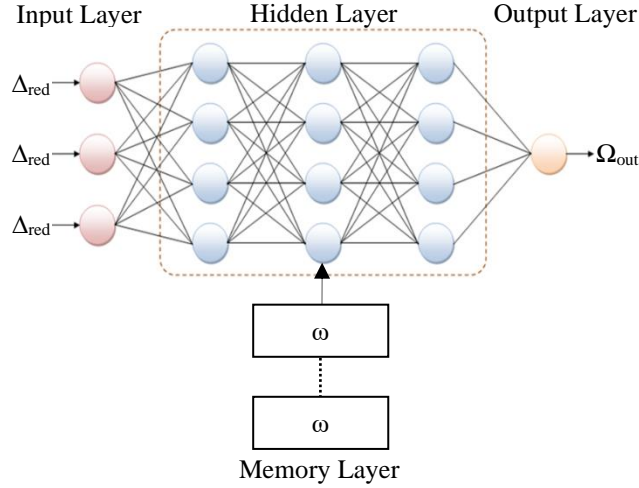
Fig. 3 Architecture of FMS-DLNN classifier

3.3.2. Phase 1- Exploration

Here, the bird finds the prey's location and moves toward the prey. The random generation of the prey's location in the search space enhances the exploration's power and aids in finding the optimal global solution. The movement toward the prey is expressed as,

$$\aleph_{i,j}^{(1)} = \begin{cases} \aleph_{i,j} + rand * (\eta_j - J \cdot \aleph_{i,j}), X_\eta < X_i; \\ \aleph_{i,j} + rand * (\aleph_{i,j} - \eta_j), else \end{cases} \tag{13}$$

Where, the newer position of the ith seed pixel in the jth decision variable in phase (1) is elucidated as $\aleph_{i,j}^{(1)}$ η_j representing the prey's location, X_η denotes their objective function value, and J symbolizes a random range [1,2].

If the objective function value is enhanced, the new position attained in this phase is accepted. The position update is represented as,

$$\aleph_i = \begin{cases} \aleph_i^{(1)}, X_i^{(1)} < X_i; \\ \aleph_i, else \end{cases} \tag{14}$$

Where, the updated position of the ith seed pixel in phase (1) is specified as $\aleph_i^{(1)}$ and $X_i^{(1)}$ symbolizes its objective function value.

3.3.3. Phase 2- Exploitation

Here, the pelicans reach the water surface, spread their wings to move the fish upwards, and gather them in the throat pouch. The local search's power is enhanced by this behavior of winging on the water's surface. This hunting behavior is described as,

$$\aleph_{i,j}^{(2)} = \aleph_{i,j} + (2 \times rand - 1) * \varepsilon_{i,j} \tag{15}$$

$$\varepsilon_{i,j} = Q * \left(1 - \frac{e}{E}\right) * \aleph_{i,j} \tag{16}$$

Where, is the newer position of the ith seed pixel in phase (2) is indicated as $\aleph_{i,j}^{(2)}$, the neighborhood radius is specified as $\varepsilon_{i,j}$, Q is a constant of value 0.2, the iteration counter is signified as e, and the total number of iterations is exemplified as E. The position update in this phase (2) is defined by,

$$\aleph_i = \begin{cases} \aleph_i^{(2)}, X_i^{(2)} < X_i; \\ \aleph_i, else \end{cases} \tag{17}$$

Where, $\aleph_i^{(2)}$ indicates the updated position of the ith seed pixel in phase (2), and $X_i^{(2)}$ is its objective function value. The best solution is updated regarding all the new positions and the objective function values produced in both phases. Until the termination criterion is satisfied, the RPO's steps are repeated. Lastly, the best candidate solution for the brain image's seed pixels is attained after several iterations. The generated seed pixels are defined as,

$$\aleph_n^s = \{\aleph_1^s, \aleph_2^s, \ldots\ldots, \aleph_N^s\} \tag{18}$$

Where, the nth number of seed pixels in the image is elucidated as $\aleph_n^s$.

3.3.4. RPO-RG

The tumor region is segmented as of the clustered image grounded on the automatically generated seeds($\aleph_n^s$). Regarding the threshold value, the input seeds are analogized with the neighboring pixels. The region selected should satisfy the criteria that the maximum mean difference betwixt a seed pixel and its neighboring pixel must be less than the threshold. After that, the similar degree of the neighboring pixel along with the generated seed pixel is computed as,

$$\mu(z) = \frac{\left\| \aleph_n^s - \varpi_{\aleph^s_{(z)}} \right\|}{\varpi_{\aleph^s_n}} where, z = 1,2, \ldots \ldots N \qquad (19)$$

Where, $\varpi_{\aleph^s_n}$ signifies the mean of the seed pixel and $\varpi_{\aleph^s_{(z)}}$ symbolizes the mean of the adjacent pixels. Afterwards, the maximum difference betwixt the seed pixel and its neighboring pixel is calculated as,

$$\lambda_{\max} = \max_{z=1}^{N} \mu(z) \qquad (20)$$

If it satisfies the above condition, the surrounding pixel is accepted by the seed pixel. Else, the neighboring pixel is considered for the next seed pixel. The regions are iteratively grown by comparison of all unallocated neighboring pixels to the seed pixel. The segmented tumor region $\left(\aleph_{seg} \right)$ is attained after performing the entire steps.

3.4. Feature Extraction

Here, the features, namely Histogram of Oriented Gradients (HOG), Local Tetra Pattern (LTP), Discrete Wavelet Transform (DWT), Gray-Level Co-occurrence Matrix (GLCM), along with the shape, are extracted from the segmented image$\left(\aleph_{seg} \right)$.

3.4.1. DWT

It provides the image's simultaneous spatial along with frequency domain information. The DWT feature in the segmented image is expressed as,

$$\aleph_{seg(DWT)} = \aleph_{seg}^w + \{ \aleph_{seg}^h + \aleph_{seg}^v + \aleph_{seg}^r \} \qquad (21)$$

Where, $\aleph_{seg}^w$ epitomizes the approximation of the segmented image, and $\aleph_{seg}^h$, $\aleph_{seg}^v$ and $\aleph_{seg}^r$ are the horizontal, vertical, and diagonal details of the image, correspondingly.

3.4.2. HOG

It is wielded for capturing gradient structure features. It works grounded on four steps, namely Orientation binning, block normalization, gradient computation, and Descriptor blocks. The mathematical representation of normalization can be expressed as,

$$\mathfrak{I} = \frac{s}{\|s\|^2 + \psi} \qquad (22)$$

Where, ψ is the constant value to avoid deviation, and s is the non-normalized vector. Lastly, the HOG feature$\left(\aleph_{seg(HOG)} \right)$ is attained from the normalization operation.

3.4.3. GLCM

It is the statistical technique for extracting texture features$\aleph_{seg(GLCM)}$ by analyzing the spatial correlation properties of gray scales in the image. The Extracted GLCM feature is expressed as,

$$\aleph_{seg(GLCM)} = \{ \aleph_{seg(con)}, \aleph_{seg(ent)}, \aleph_{seg(cor)} \} \qquad (23)$$
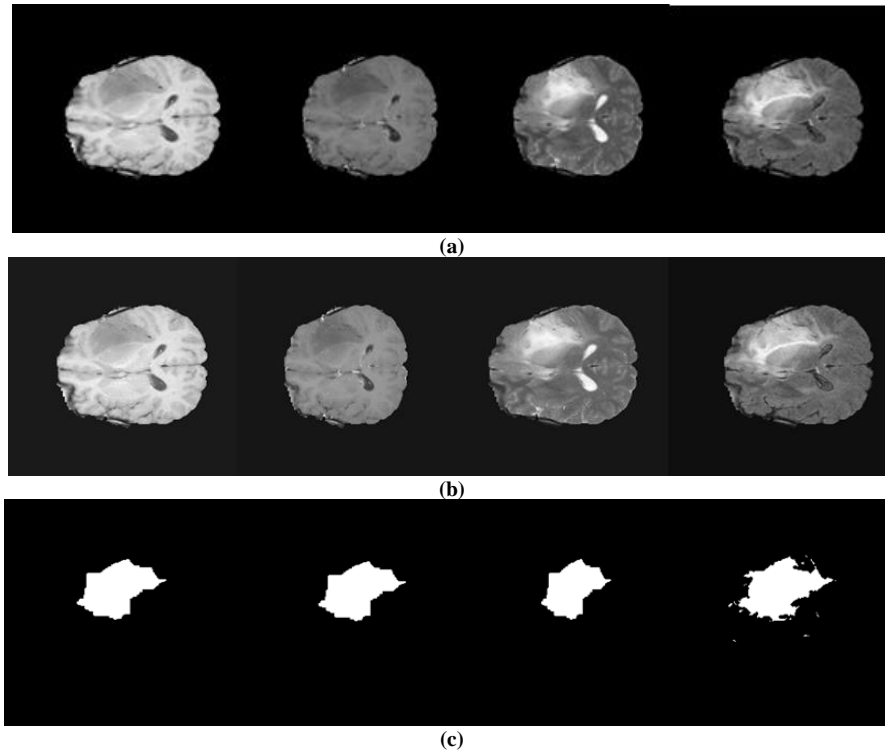
Fig. 4 (a) Input images (b) noise removed images (c) segmented images

Where, $\aleph_{seg(con)}$, $\aleph_{seg(ent)}$ and $\aleph_{seg(cor)}$ epitomizes the contrast, entropy, and correlation of the segmented image.

3.4.4. LTP

An extension of Local Binary Patterns (LBP) is the Local Ternary Patterns (LTP), which utilizes a threshold function around zero for assessing the local grayscale difference. LTP can be generated by the formula,

$$\aleph_{seg(LTP)} = \sum_{p=0}^{p-1} 2^p \, g(\ell_p - \ell_c) \tag{24}$$

Where, $g(\ell_p - \ell_c)$ it symbolizes the grayscale difference betwixt the neighborhood pixel value (ℓ_p) and centre pixel value (ℓ_c).

3.4.5. Shape

Grounded on the shape boundary information where area, parameter, and circularity are considered the major features, the shape features are extracted; also, it is computed as,

$$\aleph_{seg(shape)} = \sum_{x,y} \aleph_{seg}(x', y') \tag{25}$$

Wherein, the input segmented image with the extreme pixels is indicated as $\aleph_{seg}(x', y')$. Lastly, all the features are extracted, and the feature set is expressed as,

$$\Delta = \{\aleph_{seg(DWT)}, \aleph_{seg(HOG)}, \aleph_{seg(GLCM)}, \aleph_{seg(LTP)}, \aleph_{seg(shape)}\} \tag{26}$$

Now, the feature set (Δ), containing all the extracted features is carried out for the feature reduction process.

3.5. Feature Reduction

Here, by utilizing LFDA, the unnecessary features in the feature set (Δ) are reduced. The FDA aims to maximize the between-class variance and minimizing the within-class variance. The feature covariance matrices of both classes are presumed by the FDA, leading to a linear decision boundary that generates an error in reducing dimensionality. So, the proposed methodology utilizes a logarithmic function in the covariance matrix calculation.

LFDA attempts to find the vector that maximizes the separation betwixt the feature set's classes. LFDA is given by the weight vector θ, which maximizes the function,

$$\Delta(\theta) = \frac{\theta^T M_B \theta}{\theta^T M_W \theta} \tag{27}$$

Where, M_B and M_W are the between and within class matrices, and T epitomizes the transpose. Both the matrices are defined by,

$$M_B = log[\Theta_B * (u_1 - u_2)(u_1 - u_2)^T] \tag{28}$$
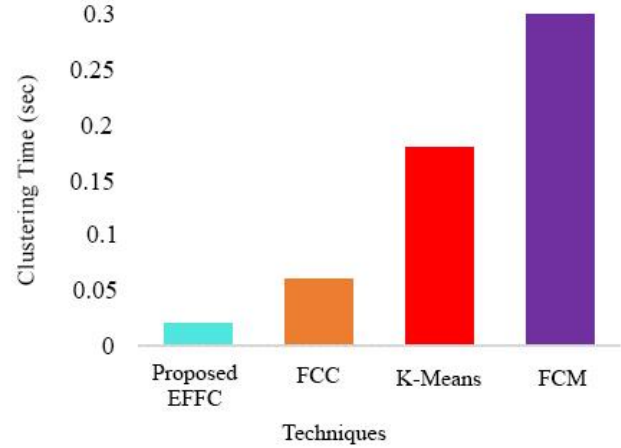
Fig. 5 Comparison of clustering time

$$M_W = log\left[\Theta_W * \sum_{i=1,2} \sum_{\vartheta \in \Delta} (\vartheta - u_1)(\vartheta - u_1)^T\right] \tag{29}$$

Where, Θ_W and Θ_B signifies the affinity matrices and u is the mean vector. The affinity matrices contain class information but do not contain locality information. Once the scatter matrices are computed, the regular LFDA Eigen problem is utilized for computing the discriminative projection. It is expressed as,

$$M_B * \Psi = \wedge M_B * \Psi \tag{30}$$

Where, Ψ symbolizes the Eigen factor. Lastly, the extracted features' dimensionality is reduced; also, the transformed feature set (Δ_{red}) is carried out for classification.

3.6. Classification

Here, for classifying the tumour's stages, the necessary features (Δ_{red}) are fed as input to the FMS-DLNN. DLNN is made up of an output layer, several HLs, along with an input layer.

Table 1. Performance analysis of the proposed GKKF technique

Techniques/Metrics	PSNR	MSE	SSIM
Proposed GKKF	70.76	0.0057	99.91
KF	57.61	0.1205	98.30
GF	53.69	0.2985	97.02
WF	45.46	1.9736	94.41

The input layer process the reduced feature set via the number of HLs; lastly, the output in the output layer is produced. In DLNN, the weight value is randomly initialized, which consumes more time for execution and may produce inaccurate outcomes.

To overcome this problem, a layer named the memory layer, which aids in selecting the weight value by utilizing previously trained data and the fuzzy rules is added to the network. Further, rather than utilizing the normal activation function, the proposed technique utilizes the Sigtan activation

function for handling the large input data and enhancing the process. Figure 3 depicts the FMS-DLNN's architecture,

Primarily, the features(Δ_{red}) are fed into the network's input layer. Utilizing the memory layer, the weight values of each layer are initialized. The memory layer encloses several weight values of the previously trained data; also, the weight values(ω) to be initialized in the proposed FMS-DLNN are selected grounded on the fuzzy rules. The weight selection is expressed as,

$$\omega \rightarrow \Xi_{out} \tag{31}$$

Wherein, Ξ_{out} signifies the memory layer's output. The weight values are selected only if the following fuzzy condition is satisfied.

$$\Phi_{out} == P_{out} \tag{32}$$

As per the above equation, the weight values relevant to that output are selected and initialized if the target output (Φ_{out}) equals the output (P_{out}) attained by the previous data in the memory layer. After that, the input values and corresponding weight values are fed into the HL, which is deeply connected with its preceding layer. The output of the HL (Ω_{hid}) is given by,

$$\Omega_{hid} = \wp(\omega * \Delta_{red} + \delta) \tag{33}$$

Here, the HL's bias value is exemplified asδ, and the activation function is specified as $\wp$. Each layer comprises many neurons, and each neuron has a function called the activation function.

Here, the Sigtan activation function is wielded for enhancing classification accuracy. The Sigtan activation function is defined by the expression,

$$\wp = \frac{e^{\Delta_{red}} - e^{-\Delta_{red}}}{1 + e^{-\Delta_{red}}} \tag{34}$$

The network comprises several HLs. The output at each layer is attained by pooling all the incoming input values. After that, the output of the HL is given to the output layer. It is expressed as,

$$\Omega_{out} = \wp(\omega * e^{-\Delta_{red}} + \delta) \tag{35}$$

Lastly, the output Ω_{out} is attained from the output layer. Thus, the proposed FMS-DLNN classifier accurately classified the stages of the BT.

4. Results and Discussions

Here, the proposed mechanism's performance is evaluated by analogizing its outcomes with other prevailing techniques.

In the working platform of MATLAB, the proposed tumor stage prediction technique is employed. The performance and comparative evaluations are executed to prove the proposed system's effectiveness.

From the collected data, 80% of images are utilized for training and 20% of images for testing. Figure 4 depicts several input MRI images (T1, T1c, T2, and FLAIR), their corresponding pre-processed, and the segmented output images.

In Figure 4(a), the input images of the four classes T1, T1c, T2, and FLAIR collected from the BraTS 2018 dataset are exposed; in Figure 4(b), the pre-processed image utilizing the GKKF technique is illustrated; in Figure 4(c), the segmented images utilizing the RPO-RG technique are displayed. The proposed model has accurately segmented the tumor region.
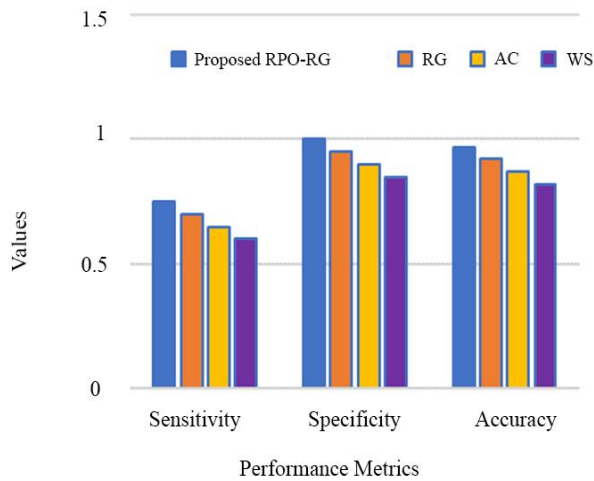
Fig. 6 Performance validation of the proposed RPO-RG algorithm
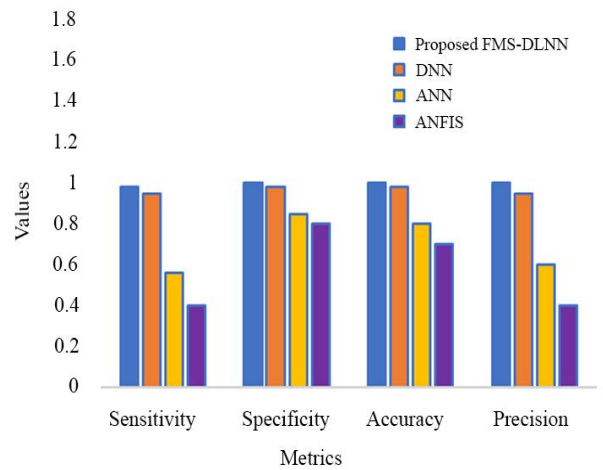
Fig. 7 Performance analysis of the proposed method
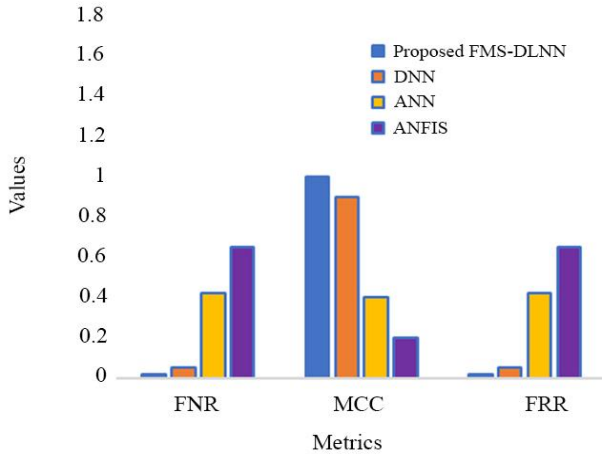
Fig. 8 Comparative analysis of the proposed and the existing methods

4.1. Database Description

The BraTS 2018 dataset's brain tumor MRI images are wielded by the proposed system. Multimodal 3D brain MRIs are enclosed by the braTS 2018 dataset, which also contains ground truth BTSs that enclose 4 MRI modalities per case (T1, T1c, T2, and FLAIR). The necrotic and non-enhancing tumor core, the peritumoral edema, and the enhancing tumor are the 3 tumor sub-regions included here.

4.2. Performance Analysis of Pre-processing

With the prevailing techniques like Kuwahara Filter (KF), Gaussian Filter (GF), along with Wiener Filter (WF), the proposed GKKF noise removal mechanism's performance is evaluated regarding the metrics like Structural Similarity Index (SSIM), Mean Square Error (MSE), together with Peak Signal-to-Noise Ratio (PSNR). Table 1 analyses the proposed GKKF and existing techniques' performance regarding some quality metrics. The proposed model's efficacy is indicated by the higher PSNR and SSIM values. The negative value is the MSE, which tends to be lower for an efficient pre-processing technique. The PSNR value attained by the proposed one is 13.15dB higher than the prevailing KF.

The SSIM value displays a greater difference of 1.61 % than the existing KF technique. Similarly, by attaining a lower MSE value when contrasted with the prevailing systems, the proposed model's MSE value also exhibits better performance. Thus, the proposed framework outperforms the conventional approaches.

4.3. Performance Analysis of Clustering

Grounded on the time consumed for clustering, the proposed EFFC's performance is assessed with the prevailing systems like Fuzzy C- Means (FCM) and K-means, along with Farthest First Clustering (FFC).

Figure 5 depicts the graphical illustration of the proposed and the prevailing approaches regarding clustering time. The proposed EFFC method takes a clustering time of 0.014485s.

The existing FFC consumed 0.06139s, the K-Means technique took 0.179249s, and the FCM system consumed 0.299207s for clustering. The above analysis exposed that the proposed EFFC yields lesser time for clustering than the prevailing techniques.

4.4. Performance Analysis of Segmentation

Concerning the metrics like specificity, recall, F-Measure, precision, Mathews Correlation Coefficient (MCC), Net Present Value (NPV), sensitivity, along with accuracy, the proposed RPO-RG's performance is assessed with the conventional approaches like RG, Watershed Segmentation (WS), and Active Contour (AC).

Grounded on specificity, sensitivity, along with accuracy, the proposed and prevailing approaches' comparative assessment is elucidated in Figure 6. These metrics' high values indicate the proposed model's high performance. 74.13% and 99.9% are the sensitivity and specificity attained by the proposed one. These values are higher than the prevailing ones.

Table 2. Performance comparison of the proposed and the existing methods

Techniques/ Metrics	Recall (%)	F-measure (%)	MCC (%)	Precision (%)	NPV (%)
Proposed RPO-RG	74.13	84.49	84.45	98.43	98.08
RG	65.14	58.80	67.03	47.22	96.71
AC	61.03	42.17	40.30	35.31	97.82
WS	57.39	28.79	27.41	19.31	97.56

Table 3. Comparative analysis of the proposed model and previous studies

Techniques/Metrics	Accuracy (%)	Dataset
Proposed FMS-DLNN	98.75	BraTS 2018
Softmax (Sharif et al., 2020)	92.5	BraTS 2018
ELM (Khan et al., 2020)	93.40	BraTS 2018
RNN (Cristin et al., 2021)	93.35	BraTS 2018

Similarly, the accuracy attained by the proposed system is 98.09%; also, it displays an improvement of 6.37% when analogized with the existing RG algorithm. Thus, it is proved that the proposed model is more effective in segmenting the tumor regions.

Table 2 exhibits the proposed RPO-RG's performance regarding the recall, F-Measure, precision, MCC, and NPV. The recall, F-measure, and Precision values of the proposed model improved by 8.99%, 25.69%, and 51.21% more than the existing RG technique. 98.08% and 84.45% are the NPV

and MCC values attained by the proposed system, while prevailing approaches provide comparatively lower performance. The proposed one performed better than the conventional frameworks in this performance comparison.

4.5. Performance Analysis of Classifier

With the prevailing approaches like Adaptive Neuro-Fuzzy Inference Systems (ANFIS), Artificial Neural Networks (ANN), along with Deep Learning Neural Networks (DLNN), the proposed FMS-DLNN's performance is analogized regarding the metrics, namely sensitivity, specificity, accuracy, precision, False Recognition Rate (FRR), False Negative Rate (FNR), MCC, and Confusion Matrix (CM).

The proposed, along with the prevailing techniques' performance, is evaluated regarding the specificity, precision, sensitivity, together with accuracy in Figure 7. The sensitivity attained by the proposed framework is 97.57%, which is higher than the prevailing DLNN, ANN, and ANFIS techniques that have 94.5%, 56%, and 38%, correspondingly. Similarly, the proposed one has specificity, accuracy, and precision of 99.16%, 98.75%, and 97.5%, which is higher when analogized with the conventional approaches. Therefore, the outcomes proved that the proposed model accurately classified the BT's stages.

Regarding FNR, MCC, along with FRR, the evaluation of the proposed technique with the prevailing mechanisms is elucidated in Figure 8. The MCC value achieved by the proposed one is 96.66%, while the prevailing approaches attain 92.66% for DLNN, 41.33% for ANN, and 17.33% for ANFIS are lower than the proposed technique. The proposed technique attained the same FNR and FRR value of 0.025. Thus, the proposed model achieved greater performance and classified the tumor stages accurately.

4.6. Comparative Analysis of Proposed Approach and Previous Approaches

The comparative assessment of the proposed FMS-DLNN and the prevailing models with the same datasets is explicated here. The comparative assessment of the proposed, along with the prevailing models, is illustrated in Table 3. When contrasted with the conventional Softmax classifier, a greater difference in accuracy by 6.70% was exhibited by the proposed mechanism. Similarly, the proposed technique performed well when analogized with the prevailing ELM and RNN models. Thus, in classifying the BT's stages, the proposed model outperforms.

5. Conclusion

This paper proposes a novel technique for BT stages prediction utilizing an FMS-DLNN classifier and automatic RPO-RG segmentation algorithm. Here, the proposed technique's performance is evaluated regarding various metrics.

The outcomes displayed that the accuracy attained by the proposed framework is 98.75% for the classifier and 98.09% for the segmentation. This exhibits the system's better performance. Moreover, for clustering, lesser time was consumed by the proposed strategy. When analogized with the prevailing approaches, the proposed one was more effective in removing the noise. Likewise, for all metrics, better performance was attained by the proposed technique.

Thus, the outcomes exhibited that the proposed technique was more efficient in classifying the BT's stages. However, the tumor type was not predicted accurately by the proposed one. For detecting the tumour type accurately, the work will be extended in the future by considering DL models trained with a larger number of layers.

References

[1] Ahmed H. Abdel-Gawad, Lobna A. Said, and Ahmed G. Radwan, "Optimized Edge Detection Technique for Brain Tumor Detection in MR Images," *IEEE Access*, vol. 8, pp. 136243–136259, 2020. [CrossRef]

[2] Mahnoor Ali et al., "Brain Tumour Image Segmentation Using Deep Networks," *IEEE Access*, vol. 8, pp. 153589–153598, 2020. [CrossRef]

[3] Javaria Amin et al., "Brain Tumor Detection by Using Stacked Autoencoders in Deep Learning," *Journal of Medical Systems*, vol. 44, p. 32, 2020. [CrossRef]

[4] S. Bhuvaneswari et al., "Disease Detection in Plant Leaf using LNet Based on Deep Learning," *International Journal of Engineering Trends and Technology,* vol. 70, no. 9, pp. 64-75, 2022. [CrossRef]

[5] Javeria Amin et al., "A New Approach for Brain Tumor Segmentation and Classification Based on Score Level Fusion Using Transfer Learning," *Journal of Medical Systems*, vol. 43, p. 326, 2019. [CrossRef]

[6] Dr R Cristin, Dr K Suresh Kumar, and Dr P Anbhazhagan, "Severity Level Classification of Brain Tumor Based on MRI Images Using Fractional-Chicken Swarm Optimization Algorithm," *Computer Journal*, vol. 64, no. 10, pp. 1514–1530, 2021. [CrossRef]

[7] Wu Deng et al., "Deep Learning-Based HCNN and CRF-RRNN Model for Brain Tumor Segmentation," *IEEE Access*, vol. 8, pp. 26665–26675, 2020. [CrossRef]

[8] Francisco Javier Díaz-Pernas et al., "A Deep Learning Approach for Brain Tumor Classification and Segmentation Using a Multiscale Convolutional Neural Network," *Healthcare*, vol. 9, no. 2, p. 153, 2021. [CrossRef]

[9]   R. Surendiran et al., " Exploring the Cervical Cancer Prediction by Machine Learning and Deep Learning with Artificial Intelligence Approaches," *International Journal of Engineering Trends and Technology,* vol. 70, no. 7, pp. 94-107, 2022. [CrossRef]

[10]   Abdu Gumaei et al., "A Hybrid Feature Extraction Method with Regularized Extreme Learning Machine for Brain Tumor Classification," *IEEE Access*, vol. 7, pp. 36266–36273, 2019. [CrossRef]

[11]   N. Pradeepa, A. Renuga Devi, and Saumiya Jose Thomas, "Survey of MRI Brain Image Segmentation Methods," *SSRG International Journal of Electronics and Communication Engineering,* vol. 2, no. 2, pp. 21-23, 2015. [CrossRef]

[12]   P. Harish, and S. Baskar, "MRI Based Detection and Classification of Brain Tumor Using Enhanced Faster R-CNN and Alex Net Model," *Materials Today: Proceedings*, 2020. [CrossRef]

[13]   Ali Hatamizadeh et al., "Swin UNETR: Swin Transformers for Semantic Segmentation of Brain Tumors in MRI Images," *Lecture Notes in Computer Science,* pp. 272–284, 2022. [CrossRef]

[14]   Dr Ravi N et al., "MRI Evaluation of Different Spectrum of Spinal Tumors," *SSRG International Journal of Medical Science,* vol. 1, no. 2, pp. 11-23, 2014. [CrossRef]

[15]   Kai Hu et al., "Brain Tumor Segmentation Using Multi-Cascaded Convolutional Neural Networks and Conditional Random Field," *IEEE Access*, vol. 7, pp. 92615–92629, 2019. [CrossRef]

[16]   Md Khairul Islam et al., "Brain Tumor Detection in MR Image Using Superpixels, Principal Component Analysis and Template Based K-Means Clustering Algorithm," *Machine Learning with Applications*, vol. 5, p. 100044, 2021. [CrossRef]

[17]   Ravi Ningappa, and Bagath Singh K, "Study of Brain Mass Lesions by MRI- On Special Sequences," *SSRG International Journal of Medical Science,* vol. 2, no. 2, pp. 1-10, 2015. [CrossRef]

[18]   Jaeyong Kang et al., "MRI-Based Brain Tumor Classification Using Ensemble of Deep Features and Machine Learning Classifiers," *Sensors*, vol. 21, no. 6, p. 2222, 2021. [CrossRef]

[19]   Gökay Karayegen, and Mehmet Feyzi Aksahin, "Brain Tumor Prediction on MR Images with Semantic Segmentation by Using Deep Learning Network and 3D Imaging of Tumor Region," *Biomedical Signal Processing and Control,* vol. 66, p. 102458, 2021. [CrossRef]

[20]   Sindhia, Ramanitharan, Shankar Mahalingam, and Soundarya Prithiesh, "Brain Tumor Detection Using MRI by Classification and Segmentation," *SSRG International Journal of Medical Science,* vol. 6, no. 3, pp. 12-14, 2019. [CrossRef]

[21]   Nivea Kesav, and M.G. Jibukumar, "Efficient and Low Complex Architecture for Detection and Classification of Brain Tumor using RCNN with Two Channel CNN," *Journal of King Saud University - Computer and Information Sciences*, vol. 34, no. 8, pp. 6229–6242, 2022. [CrossRef]

[22]   Amjad Rehman Khan et al., "Brain Tumor Segmentation Using K-Means Clustering and Deep Learning with Synthetic Data Augmentation for Classification," *Microscopy Research and Technique,* vol. 84, no. 7, pp. 1389-1399, 2021. [CrossRef]

[23]   Muhammad Attique Khan et al., "Multimodal Brain Tumor Classification Using Deep Learning and Robust Feature Selection: A Machine Learning Application for Radiologists," *Diagnostics*, vol. 10, no. 8, p. 565, 2020. [CrossRef]

[24]   R. Surendiran et al., "Effective Autism Spectrum Disorder Prediction to Improve the Clinical Traits using Machine Learning Techniques," *International Journal of Engineering Trends and Technology,* vol. 70, no. 4, pp.343-359, 2022. [CrossRef]

[25]   Muhammad Waqas Nadeem et al., "Brain Sciences Brain Tumor Analysis Empowered with Deep Future Challenges," *Brain Sciences,* vol. 10, no. 2, p. 118, 2020. [CrossRef]

[26]   P. Nagaraj et al., "Programmed Multi-Classification of Brain Tumor Images Using Deep Neural Network," *Proceedings of the International Conference on Intelligent Computing and Control Systems,* pp. 865–870, 2020. [CrossRef]

[27]   Fareed M.mohammed, Mustafa M.Essa, and Ahmed W. Maseer, "Comparison between MRI and CT-Scan in Diagnosis the Brain Tumor Images," *SSRG International Journal of Medical Science,* vol. 6, no. 5, pp. 1-4, 2019. [CrossRef]

[28]   Bing Niu et al., "Glioma Stages Prediction Based on Machine Learning Algorithm Combined with Protein-Protein Interaction Networks," *Genomics,* vol. 112, no. 1, pp. 837–847, 2020. [CrossRef]

[29]   Neelum Noreen et al., "A Deep Learning Model based on Concatenation Approach for the Diagnosis of Brain Tumor," *IEEE Access*, vol. 8, pp. 55135–55144, 2020. [CrossRef]

[30]   Hasnain Ali Shah et al., "A Robust Approach for Brain Tumor Detection in Magnetic Resonance Images Using Finetuned EfficientNet," *IEEE Access*, vol. 10, pp. 65426–65438, 2022. [CrossRef]

[31]   Muhammad Irfan Sharif et al., "Active Deep Neural Network Features Selection for Segmentation and Recognition of Brain Tumors Using MRI Images," *Pattern Recognition Letters*, vol. 129, pp. 181–189, 2020. [CrossRef]

[32]   Ankit Vidyarthi et al., "Machine Learning Assisted Methodology for Multiclass Classification of Malignant Brain Tumors," *IEEE Access*, vol. 10, pp. 50624–50640, 2022. [CrossRef]

[33]   R. Tamilaruvi et al., "Brain Tumor Detection in MRI Images using Convolutional Neural Network Technique," *SSRG International Journal of Electrical and Electronics Engineering,* vol. 9, no. 12, pp. 198-208, 2022. [CrossRef]